

## Asymmetries in 100 MeV $\pi^+/\pi^-$ - $^3\text{He}$ elastic scattering

B. Larson,<sup>1,2</sup> O. Häusser,<sup>2,3</sup> J. Alster,<sup>4</sup> M. Bahrami,<sup>2</sup> E. J. Brash,<sup>2,\*</sup> W. J. Cummings,<sup>2</sup> P. P. J. Delheij,<sup>3</sup>  
R. Henderson,<sup>3</sup> D. Ottewell,<sup>3</sup> A. Rahav,<sup>2</sup> S. Ram,<sup>4</sup> M. C. Vetterli,<sup>3</sup> and D. M. Whittal<sup>3,†</sup>

<sup>1</sup>Ohio University, Athens, Ohio 45701

<sup>2</sup>Simon Fraser University, Burnaby, British Columbia, Canada V5A 1S6

<sup>3</sup>TRIUMF, 4004 Wesbrook Mall, Vancouver, British Columbia, Canada V6T 2A3

<sup>4</sup>Tel-Aviv University, Ramat Aviv, Israel 69978

(Received 13 September 1993; revised manuscript received 27 December 1993)

We have measured cross sections and analyzing powers for  $\pi^+$  and  $\pi^-$  elastic scattering from a polarized  $^3\text{He}$  target at  $T_\pi = 100$  MeV. Measurements have been made over an angular range of  $60^\circ$  to  $110^\circ$  which extends over the region of the cross section minimum where spin effects in  $\pi$ -nucleus scattering are predicted to be largest. This is evident from the large value of  $A_y$  observed in  $\pi^+$  scattering from  $^3\text{He}$  near  $\theta_{\text{lab}} = 80^\circ$ . The  $A_y$  data for both  $\pi^+$  and  $\pi^-$  scattering are qualitatively reproduced by a schematic PWIA model; however, agreement with the data is significantly improved when a full nonlocal DWIA reaction model employing realistic three-body wave functions is used. The asymmetry in  $\pi^-$ - $^3\text{He}$  scattering resembles the asymmetry for  $\pi^-$  scattering from a free neutron near the cross section minimum and is about half that for  $\pi^+$  scattering.

PACS number(s): 25.10.+s, 24.70.+s, 25.80.Dj, 27.10.+h

### I. INTRODUCTION

Within the last two decades much work has been done to further our understanding of the spin dependent part of the pion-nucleus interaction using pion elastic and charge exchange scattering as the tools. Prior to this attention had been focused primarily on nuclei with  $J = 0$  where effects due to Fermi motion of the target nucleons, Pauli blocking, and off-shell extrapolation of the elementary  $\pi$ - $N$   $t$  matrix [1,2] were investigated. These initial studies provided no information on the spin dependent part of the pion-nucleus interaction. More recently, a number of microscopic momentum space optical potential calculations [3–9] have been developed for nuclei with nonzero spin and isospin. These calculations preserve the full spin-isospin dependence of the elementary  $\pi$ - $N$  amplitudes which contain a complex spin independent (non-spin-flip) and a complex spin dependent (spin-flip) amplitude for each isospin channel. It was also clear long ago that, in the case of elastic scattering, studies using light nuclei would be of great value in examining the spin dependence of such effects. Since spin dependence in elastic scattering is often due to a single valence nucleon, its effects are reduced in magnitude by approximately  $1/A$  relative to spin independent phenomena.

Since it is only recently that polarized nuclear ( $A > 2$ ) targets have been developed [10–12], the vast majority of information on spin dependence in the pion-nucleus inter-

action has been derived from cross section measurements on odd- $A$  nuclei, perhaps most notably on the  $^3\text{He}$  nucleus. Accurate cross section measurements for  $\pi^\pm$ - $^3\text{He}$  elastic scattering at energies from 30 to 300 MeV have existed for almost ten years [13–15]; however such measurements are only sensitive to the strength of the spin-flip part of the interaction near the cross section minimum where the spin-flip amplitude is at a maximum. The degree to which the minimum is “filled in” is indicative of the strength of the spin-flip term. Measurements of the asymmetry parameter,  $A_y$ , in pion-nucleus elastic scattering provide valuable new information on the spin-flip piece of the interaction since  $A_y$  depends on the interference between the spin-flip and nonflip amplitudes whereas the cross section depends on their incoherent sum.

For spin-1/2 targets in the  $1p$  shell [10,11],  $^{13}\text{C}$  and  $^{15}\text{N}$ , relatively small asymmetries have been observed. A conclusive interpretation of these measurements is furthermore made difficult by uncertainties in standard wave functions for the nuclear ground state which give a poor description of the measured magnetic form factors, e.g., in  $^{13}\text{C}$  [16] at momentum transfers  $q \sim 2 \text{ fm}^{-1}$ . In contrast to the  $p$ -shell nuclei, the  $^3\text{He}$  nuclear wave function can be calculated with good accuracy from the Faddeev equations using realistic  $NN$  potentials as input [17]. Therefore, for  $^3\text{He}$  the nuclear structure uncertainties are almost negligible relative to  $p$ -shell nuclei. The  $^3\text{He}(\pi, \pi)$  reaction is thus an ideal probe of the detailed spin dependence of the spin-0 – spin-1/2 nuclear scattering amplitude [4–9].

Experimentally, asymmetry measurements with secondary beams (with pion fluxes of  $10^6$ – $10^7 \text{ s}^{-1}$ ) have only recently become feasible due to the development of an optically pumped high density polarized  $^3\text{He}$  target at TRIUMF [12]. The first measurements of this type

\*Present address: Los Alamos Natl. Laboratory, Los Alamos, NM 87545.

†Permanent address: National Accelerator Centre, Faure, 7131, South Africa.

were reported in 1991 [18] where a very large asymmetry was observed in  $\pi^+{}^3\text{He}$  elastic scattering near  $\theta_{\text{lab}} = 80^\circ$ . These first measurements at  $60^\circ$ ,  $80^\circ$ , and  $100^\circ$  laboratory angle for the  $\pi^+{}^3\text{He}$  reaction only, represent the first phase of the experiment described in this paper. The “second phase” includes asymmetry measurements for  $\pi^+{}^3\text{He}$  scattering at  $70^\circ$ ,  $90^\circ$ , and  $110^\circ$  as well as a remeasurement at  $80^\circ$  and asymmetry measurements for the  $\pi^-{}^3\text{He}$  reaction at six angles ranging from  $60^\circ$  to  $110^\circ$ .

In the following section a detailed description of our experimental setup is given followed by a discussion of the data analysis in Sec. III. In Sec. IV our data are compared with two reaction model calculations. The first is a full nonlocal distorted-wave impulse approximation (DWIA) calculation which utilizes Faddeev wave functions for the nuclear structure [9]. The second is a plane-wave impulse approximation (PWIA) calculation [19] in which the  $\pi N$  amplitudes are given as products of the elementary  $\pi N$  amplitudes and a simple form factor which cancels out when the asymmetry is calculated. A brief summary is given in the final section.

## II. THE EXPERIMENT

The experiment was carried out at the M11 pion channel at TRIUMF using an optically pumped polarized  ${}^3\text{He}$  target. Momentum analysis of the scattered pions was performed with the quadrupole-quadrupole-dipole (QQD) spectrometer system [20].

### A. General layout of the experiment

A schematic of the experimental layout is shown in Fig. 1. The pion beam traversed two sets of multiwire proportional chambers (MWPC’s) and a small scintillator (B1)

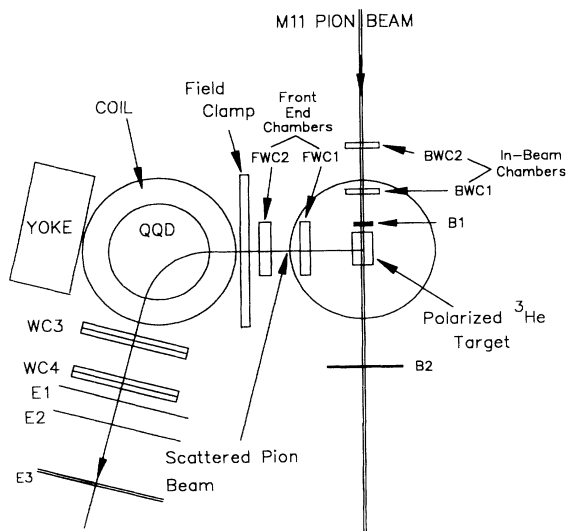


FIG. 1. An overview of the experimental layout.

before entering the  ${}^3\text{He}$  target. Pions that scattered in the region of the  ${}^3\text{He}$  target were tracked using two more sets of MWPC’s located between the target and the entrance to the QQD. Two sets of delay line wire chambers were located at the exit of the QQD and were used to calculate the focal plane coordinate for the scattered pions. The final elements of the setup are the three scintillators  $E1$ ,  $E2$ , and  $E3$ . They were used to provide a clean trigger and particle identification through energy loss and time of flight discrimination.

### B. The polarized ${}^3\text{He}$ target

A detailed discussion of the TRIUMF polarized  ${}^3\text{He}$  target can be found elsewhere [12]. A depiction of the target apparatus is shown in Fig. 2. Briefly, the target used in phase two consisted of an 8 cm long  $\times$  2.5 cm inner diameter glass cell which contained 10 atm of  ${}^3\text{He}$  gas, a few mg of Rb alkali metal, and  $\approx 100$  Torr of  $\text{N}_2$  quench gas. The glass cell was mounted in an oven made of the polyimide VESPEL. Windows consisting of two layers of  $25\ \mu\text{m}$  kapton separated by an air gap of 1.2 cm were used to reduce heat loss and thermal gradients within the oven while contributing a minimal amount to the energy loss of the incident and scattered pions. The oven was operated at a temperature of 450 K to produce a Rb density of  $\sim 4 \times 10^{14}\ \text{cm}^{-3}$ . About 7 W of circularly polarized photons ( $\lambda = 795.8\ \text{nm}$ ) were used to optically pump Rb via the  $D1$  line. A vertical holding field of 3 mT was produced by a set of 1 m diameter Helmholtz coils.

The target polarization produced by the Fermi contact hyperfine interaction during Rb- ${}^3\text{He}$  spin exchange collisions could be reversed and analyzed by adiabatic fast passage NMR. The NMR signal induced by the rotating  ${}^3\text{He}$  magnetic moment was compared to that from a water sample of similar geometry to obtain an absolute value of the polarization. Because of the weakness of the

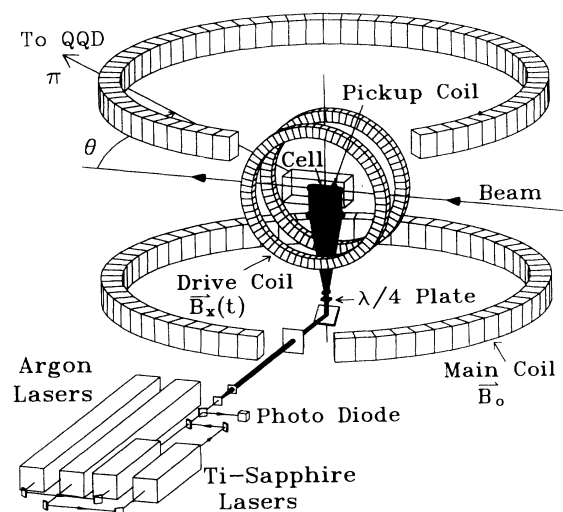


FIG. 2. The TRIUMF optically pumped  ${}^3\text{He}$  target setup.

TABLE I. Cross sections and analyzing powers for 100 MeV  $\pi^+$ - $^3\text{He}$  elastic scattering.

$\theta_{\text{c.m.}}$ (deg)	$(d\sigma/d\Omega)_{\text{c.m.}}$ (mb/sr)	$A_y$
64.0	$1.8 \pm 0.08 \pm 0.45$	$0.04 \pm 0.09 \pm 0.02$
75.4	$0.86 \pm 0.09 \pm 0.11$	$0.69 \pm 0.17 \pm 0.035$
85.0	$1.07 \pm 0.10 \pm 0.13$	$0.80 \pm 0.094 \pm 0.04$
95.6	$1.83 \pm 0.11 \pm 0.22$	$0.52 \pm 0.09 \pm 0.03$
104.5	$2.1 \pm 0.06 \pm 0.53$	$0.38 \pm 0.06 \pm 0.04$
115.3	$2.94 \pm 0.14 \pm 0.33$	$0.25 \pm 0.08 \pm 0.013$

water signal [it is smaller than the  $^3\text{He}$  signal by a factor of  $(3.71 \times 10^4)pP$  where  $p$  and  $P$  are the  $^3\text{He}$  pressure and polarization, respectively], and also because of a significant temperature dependence in the induced NMR signal, a systematic uncertainty of  $\Delta P_t/P_t = 0.07$  has been adopted for the absolute  $^3\text{He}$  polarization during the first phase of the experiment. A reduction in the number of windings on the NMR pickup coil greatly reduced the temperature sensitivity of the induced signal and allowed a determination of the proton NMR signal to an accuracy of less than 5%. Thus an uncertainty of  $\Delta P_t/P_t = 5\%$  is applied to the data taken during the second phase of the experiment. This uncertainty is included in the overall systematic uncertainties for  $A_y$  quoted in Tables I and II.

A significant improvement in laser power stability was also gained between the first and second phases of the ex-

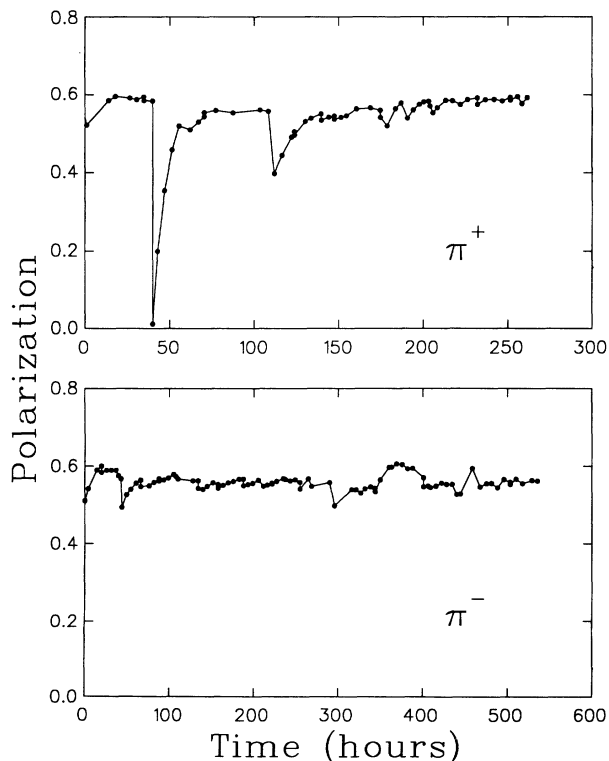


FIG. 3. The variation of the  $^3\text{He}$  polarization as a function of time throughout the course of this experiment.

TABLE II. Cross sections and analyzing powers for 100 MeV  $\pi^-$ - $^3\text{He}$  elastic scattering.

$\theta_{\text{c.m.}}$ (deg)	$(d\sigma/d\Omega)_{\text{c.m.}}$ (mb/sr)	$A_y$
65.1	$1.8 \pm 0.16 \pm 0.22$	$0.32 \pm 0.10 \pm 0.06$
75.4	$1.04 \pm 0.07 \pm 0.12$	$0.36 \pm 0.12 \pm 0.02$
85.6	$0.96 \pm 0.05 \pm 0.11$	$0.55 \pm 0.09 \pm 0.03$
95.6	$0.97 \pm 0.06 \pm 0.12$	$0.41 \pm 0.11 \pm 0.06$
105.5	$1.1 \pm 0.09 \pm 0.13$	$0.19 \pm 0.13 \pm 0.10$
115.3	$1.21 \pm 0.09 \pm 0.15$	$0.28 \pm 0.13 \pm 0.10$

periment. The Ti:sapphire lasers were sealed and purged with filtered air which reduced by an order of magnitude the frequency with which optical pumping had to be interrupted to allow for cleaning of the laser optics. The first phase of the experiment employed a target of 7.03 standard atm pressure and a typical polarization of 45–55%. The second phase employed a slightly smaller target of 10 standard atm pressure and typical polarizations of 55–60%. A plot of the  $^3\text{He}$  polarization as a function of time is given in Fig. 3 for the second phase of the experiment only.

### C. The spectrometer and detectors

Two modifications were necessary to make the QQD compatible with the polarized  $^3\text{He}$  target. The first was the removal of both quadrupoles to satisfy the spatial constraints imposed by the target and also to limit magnetic field gradients at the target to  $< 3 \mu\text{T cm}^{-1}$ . The second was the installation of a field clamp at the entrance to the dipole to further reduce magnetic field gradients at the target. These modifications reduced the angular acceptance in the vertical (nonbend) plane to  $\approx 3.5^\circ$  whereas the spectrometer angular acceptance in the horizontal (bend) plane was  $7^\circ$ .

Since the QQD optics was changed substantially by removal of the two front end quadrupoles it was necessary to recalibrate the scattered pion momentum as a function of focal plane position. The calibration was obtained by scattering a 100 MeV  $\pi^+$  from a  $300 \text{ mg/cm}^2 \text{ CH}_2$  target at angles from  $50^\circ$  to  $110^\circ$  thereby sweeping the  $\pi^+$ - $P$  elastic peak across the focal plane. This also served as data for normalization of the  $^3\text{He}$  cross sections.

The small 17 mm diameter scintillator ( $B1$ ) placed directly upstream of the target cell defined the active area of the target and measured the total beam charge incident on the target cell. The signal from  $B1$  was used as the common start signal for all other electronics and defined the trigger timing.

Tracking to the target was provided by four sets of MWPC's. Two sets were placed directly in the beam (BWC's) and the other two were located between the target and the QQD (FWC's). The MWPC's are specifically designed to operate efficiently at the 1–10 MHz rates realized for chambers located directly in the beam. The wire arrangement in these chambers consists of a plane of an-

ode wires with a cathode foil plane on either side which is maintained at a negative high voltage. The anode signals from each individual wire are fed into separate preamplifiers located on the wire chamber. The preamplified signals are then sent into 16-channel discriminator cards which form the front end of the PCOS III readout system. The discriminated signals are sent into 32-channel encoder units. A crate readout controller reads only the encoder units which register a hit and encodes the addresses of all wires that were hit. The addresses are then buffered for readout by CAMAC.

Since there is no drift time interpolation with this system, spatial resolution is limited to the 0.76 mm wire spacing. The first beam chamber (BWC1 in Fig. 1) is located 341 mm from the target center with the separation between the chambers being about 230 mm. The corresponding resolution for tracking the beam to the target is about 1 mm in both the horizontal and vertical directions and is limited by multiple scattering in the target and trigger scintillator.

The front end chambers (FWC's) are virtually identical in construction and readout to the in-beam chambers (BWC's) previously described, the only differences being that the FWC's are much larger ( $25.6 \times 25.6$  cm) and have a slightly larger (1 mm) wire spacing. Both sets of chambers employ the PCOS III readout system. A useful feature of the 32-channel encoder modules is the prompt "OR" signal which can be obtained by wiring together the inputs for all of its 32 channels. This feature allowed us to incorporate the FWC's in the trigger and eliminate the need for an additional plastic scintillator between the target and the QGD, thus keeping multiple scattering to a minimum.

The first FWC was located 362 mm from the target center with the separation between the chambers being 300 mm. The tracking resolution from this side of the target was also about 1 mm in both the horizontal and vertical directions. Only the detector areas which were compatible with the spectrometer acceptance were instrumented. The traceback from the FWC's in conjunction with that from the in-beam chambers was used to construct a three-dimensional image of the target and subsequently exclude events which were observed to come from the VESPEL oven and the glass vessel which contained the  $^3\text{He}$ . Together the four sets of MWPC's provide ray tracing to the target with 1–2 mm resolution.

### III. DATA ANALYSIS

Data were acquired and written to magnetic tape using TRIUMF's VDACS data acquisition system. The NOVA software package was used for both the on-line and off-line analysis of the data. The hardware trigger for this experiment consisted of a coincidence between the beam scintillator  $B1$ , all of the back plane scintillators,  $E1$ ,  $E2$ , and  $E3$ , and an "OR" of the  $Y$  planes of the front end chambers. This condition was sufficient to constrain the triggering particles to be pions or muons originating in the vicinity of the  $^3\text{He}$  target cell. Few of the muons have sufficient momentum to be transported through the QGD

however. More stringent requirements on the scattering vertex are described below.

#### A. Background sources

The initial software filters applied in the playback of the data were that the particles satisfy time of flight and energy loss criteria. The time of flight relative to the front end scintillator  $B1$  versus the energy loss in scintillator  $E3$  is shown in Fig. 4. It is clear that there is little contribution from particles other than pions which are contained inside the rectangular box. The small locus at longer time of flight arises from muons which decayed in flight part way through the spectrometer. The loci at very short time of flight are probably due to random coincidences and comprise less than 1% of the total events. The other constraint imposed on the "raw" data was that the event be composed of a single hit in all 12 of the wire chamber planes. Since the number of events where more than one hit was recorded in the "in-beam" chambers was substantial ( $\approx 10\%$  for the  $\pi^+$  data), these multiple track events were recovered in the cases where at most two tracks were recorded. In these cases, the track which came closest to intersecting the track from the FWC's was selected.

The most important cuts for the reduction of background under the  $^3\text{He}$  elastic peak are those involving the scattering vertex position. The scattering vertex is given by the midpoint of the line joining the vectors which describe the incoming and outgoing pion trajectories at their points of closest approach. Accurate determination of the vertex within the target was essential for rejection of events which originated in the glass end caps and side walls of the target cell. A full three-dimensional vertex reconstruction was used in order to optimize the traceback resolution.

Two different projections of the target image, a one-dimensional projection of the target cell onto the beam axis ( $z$  coordinate) and a two-dimensional projection of the cell onto the plane perpendicular to the beam axis ( $x$ - $y$  plane) were used to identify the  $^3\text{He}$  events. These projections are shown in Fig. 5. Software cuts on  $z$  elimi-

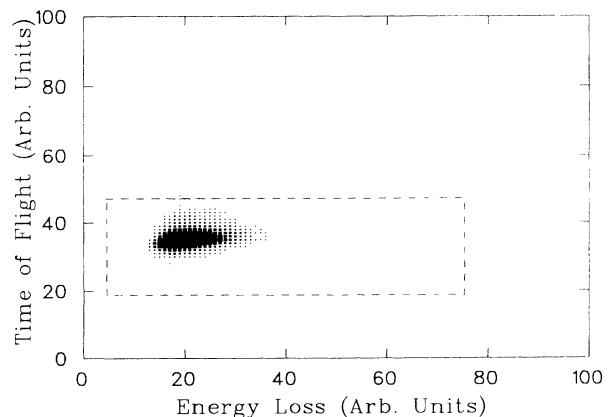


FIG. 4. The time of flight plotted against the energy loss in scintillator  $E3$  of Fig. 1.

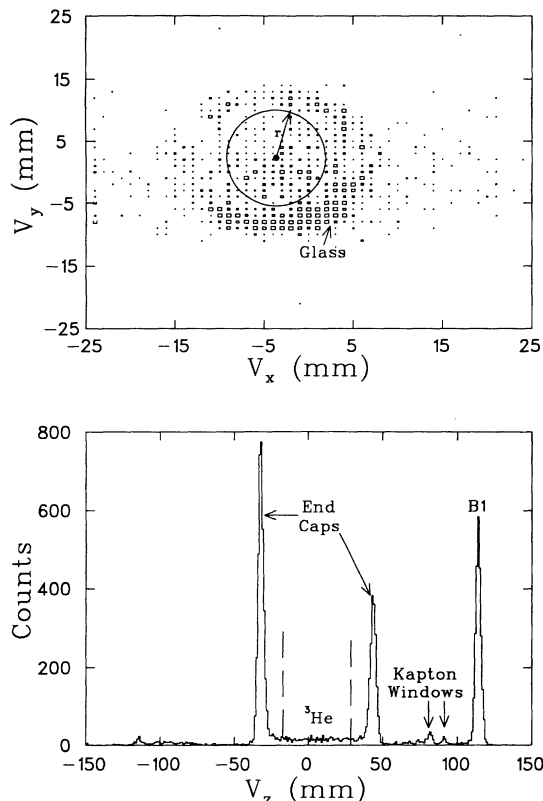


FIG. 5. Events from the  $^3\text{He}$  target cell projected onto the plane normal to the beam axis (top) and onto the beam axis (bottom).

nated events from the end caps while a cut on the radius coordinate ( $r = \sqrt{x^2 + y^2}$ ) eliminated events from the cell walls. With the cuts from the tracking chambers the useable  $^3\text{He}$  target length was 4.5 cm which corresponds to an areal density of  $8.5 \times 10^{20}$  atoms  $\text{cm}^{-2}$  (4.26 mg  $\text{cm}^{-2}$ ) for phase one or  $1.25 \times 10^{21}$  atoms  $\text{cm}^{-2}$  for phase two.

Since events were only accepted for a limited value of the radius, which is smaller than the radius constraint of scintillator B1, the total number of beam particles measured by B1 had to be adjusted. This was done using data taken with the  $\text{CH}_2$  target. Using this method it was found that at least 85% of the beam incident on B1 was within an acceptable radius from the beam axis.

### B. The focal plane momentum calibration

The two MWPC's (FWC1 and FWC2) located between the target and the spectrometer together with two additional chambers (WC3 and WC4) located at the back plane of the spectrometer allowed the focal plane of the dipole to be determined. An outline of the focal plane geometry is presented in Fig. 6. In terms of the wire chamber coordinates  $X_3$  and  $X_4$  which are the horizontal coordinates for WC3 and WC4 of Fig. 2, the raw focal plane position  $X_F$  is defined as

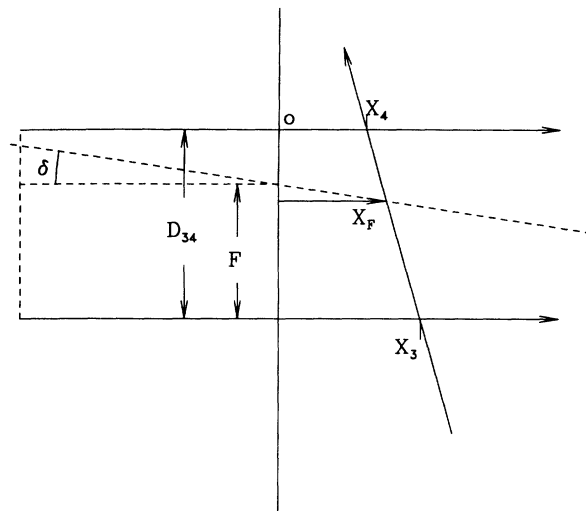


FIG. 6. An illustration of the QGD focal plane coordinate calculation.

$$X_F = \frac{X_4 \cdot D_{34} + [(D_{34} - F) \cdot (X_3 - X_4)]}{D_{34} - (X_3 - X_4) \cdot \tan \delta}, \quad (1)$$

where the distance from the focal plane to the mid-point of WC3,  $F$ , and the slope of the focal plane relative to WC3,  $\delta$ , were determined using  $^{12}\text{C}$  elastic scattering data taken at three magnetic field settings. For the QGD with no quadrupoles the values of these parameters are  $F = 234$  mm and  $\delta = -60.2^\circ$ . The focal plane exists only for scattered pions which come from a point source (a thin target) and exhibit negligible momentum spread over the range of scattering angles accepted by the spectrometer. The pions scattered from  $^3\text{He}$  however, have a significant momentum spread over the  $\sim 7^\circ$  horizontal ( $\theta$ ) and  $\sim 3^\circ$  vertical ( $\phi$ ) acceptance. This dependence is corrected for up to second order in  $\theta$  and, only in second order in  $\phi$ , since the range of  $\phi$  is centered on 0. A correction was also made for the target position  $V_z$  at which the pion originated. The corrected focal plane coordinate was parametrized as

$$PCX_F = A\theta + B\theta^2 + C\phi^2 + DV_z,$$

where the parameters  $A$ - $D$  were determined empirically.

Elastic  $\pi$ - $P$  scattering was then measured at several angles from  $50^\circ$  to  $110^\circ$  to provide both a momentum calibration of the focal plane and an acceptance versus  $X_F$  profile. The momentum calibration assumes that the focal plane coordinate is linear in momentum, i.e.,  $p = AX_F + B$ . The acceptance scan is used for normalization of the  $^3\text{He}$  cross sections and is discussed in the following section.

### C. QGD acceptance correction

The acceptance correction applied to our data was obtained by measuring  $\pi$ - $p$  elastic scattering cross sections

at several points across the focal plane and comparing them to previous more accurate data. Since the  $^3\text{He}$  angular distributions were obtained at a single magnetic field setting, the elastic peaks for different angles also occur at different points on the focal plane. The  $\pi$ - $p$  cross sections used for comparison come from the Arndt phase shift solution SM90. A quadratic function was fitted to these acceptance data, and was used to define an acceptance correction for any focal plane position  $X_F$ . The relative acceptance is shown as a function of focal plane position in Fig. 7 where the arrows indicate the range of  $X_F$  spanned by the  $^3\text{He}$  data.

The  $\pi^-$ - $p$  cross sections were too small to allow a statistically significant acceptance scan to be obtained during the course of the experiment. Instead, a single normalization factor between  $\pi^+$  and  $\pi^-$  scattering was obtained by comparing measured  $\pi^-$ - $^{12}\text{C}$  and  $\pi^+$ - $^{12}\text{C}$  cross sections at one angle and renormalizing the  $\pi^+$ - $p$  acceptance curve accordingly.

#### D. Calculation of the cross section and spin observables

The differential cross section for scattering can be written

$$\frac{d\sigma}{d\Omega} = \frac{N_s A}{N_i N_o \tau} \frac{1}{\Delta\Omega}, \quad (2)$$

where  $N_i$  is the number of incident particles,  $A$  is the atomic weight of the target nuclei,  $N_o$  is Avogadro's number, and  $\tau$  is the areal density of the target. The accepted solid angle,  $\Delta\Omega$ , is determined by software cuts on the horizontal and vertical scattering angles. The true number of scattered particles is inferred from the actual measured yields by

$$N_s = \frac{N_{\text{meas}}}{lt \cdot A_c \cdot \epsilon \cdot M_s \cdot S_f \cdot B}, \quad (3)$$

where  $lt$  is the computer livetime which was typically about 0.85,  $A_c$  is the acceptance or "normalization" correction, and  $\epsilon$  is the total wire chamber efficiency (typically  $\sim 0.4$ – $0.5$ ). The fraction of events whose scattering

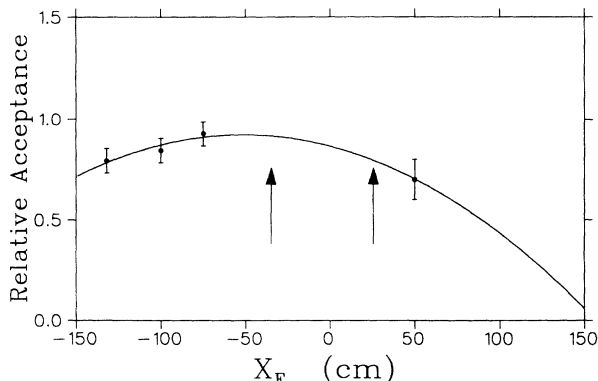


FIG. 7. The QQD acceptance as a function of the focal plane position.

vertex could be located to within  $\pm 2$  mm,  $M_s$ , accounts for losses due to multiple scattering. There is additionally the constraint that the vertical (nonbend plane) scattering angles for pions entering the QQD and those exiting the QQD be approximately the same. The pion survival fraction over the 1.6 m flight path from FWC2 to WC4 is  $S_f$ . For pions scattered from hydrogen at an angle of  $50^\circ$  the time of flight over this distance is about  $4.8 \times 10^{-9}$  s (in the pion frame). The pion mean lifetime  $\tau = 26$  ns implies a pion survival fraction  $e^{-4.8/26} = 0.83$ . It is assumed that all pions which decay prior to FWC2 will be eliminated by the traceback, and those which decay after WC4 will still be detected in the scintillators. Some pion decays will be accounted for in the multiple scattering corrections. The loss of beam flux due to the constraint on the radius coordinate is compensated by the factor  $B$ .

Only statistical uncertainties are assumed for the live-time, efficiency, and the multiple scattering corrections. They are typically small and amount to  $\sim 1\%$ . A systematic uncertainty of  $\pm 8\%$  for the pion survival fraction was estimated from the difference between the flight time from FWC2 to WC4 and that from the target to WC4. The uncertainty in the  $\text{CH}_2$  areal density which is included in the error estimate of the  $^{12}\text{C}$  and  $^1\text{H}$  cross sections is about 2%. The statistical uncertainties for the  $\text{CH}_2$  measurements are typically about 5%. The overall uncertainty in the measurement of the  $^{12}\text{C}$  and  $^1\text{H}$  cross sections, including a 4% uncertainty in the solid angle  $\Omega$ , is then typically 10–11%.

Determination of the  $\pi^+$ - $p$  cross sections at angles where the scattered pion momentum is close to the central momentum of the QQD yields values which agree with the SM90 phase shifts to within the above uncertainty. The  $\pi^-$ - $^3\text{He}$  cross sections are multiplied by factors  $\sigma_{\text{SM90}}/\sigma_{\text{meas}}$  which vary from 1.09 to 1.25 over the angular range of the  $^3\text{He}$  data. The uncertainty adopted for the  $^3\text{He}$  normalization factor has a component from the uncertainty in the SM90 phase shift solution ( $\sim 6\%$ ) and one from the uncertainty in the measured  $^{12}\text{C}$  and hydrogen cross sections,  $\sim 10\%$ . An uncertainty of 12% was therefore adopted as the acceptance correction factor for the  $^3\text{He}$  cross sections. This is given as the systematic uncertainty in the  $^3\text{He}$  cross section in Tables I and II.

Normalized yield spectra for target spins up ( $\sigma_\uparrow$ ), down ( $\sigma_\downarrow$ ), and the difference taken at  $\theta_{\text{lab}} = 80^\circ$  are shown in Fig. 8. In extracting the counts contained in the peaks, two different background shapes were assumed for the region of the elastic peak, a constant flat background and a linear background with a small slope. The systematic uncertainties for  $A_y$  quoted in the tables include the uncertainty in the  $^3\text{He}$  polarization given above as well as an estimate of the consistency of the two background subtraction methods. Since the ratio of peak counts to background counts is large, this contribution to the systematic uncertainty is typically much less than that due to the uncertainty in the target polarization. The target polarization labels ( $\uparrow$  and  $\downarrow$ ) refer to a coordinate system in which the scattered pions are detected on the left side of the beam. The difference spectrum shown in Fig. 8 (bottom frame) is proportional to analyzing power multiplied by the unpolarized cross section

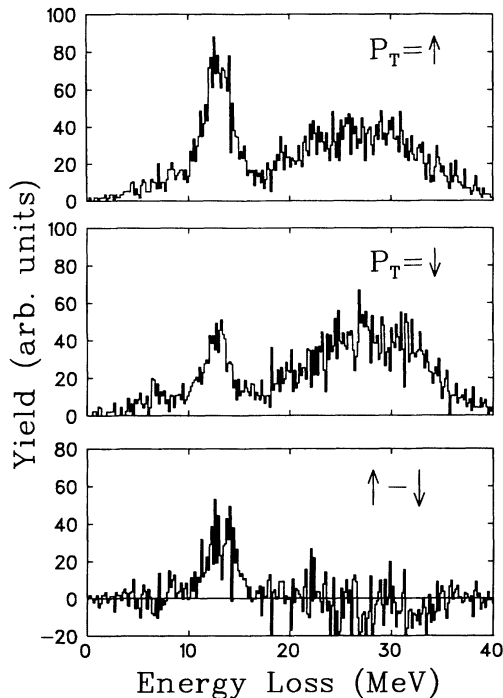


FIG. 8. Normalized yields vs energy loss for the target spin up (top) and down (middle) projections. The difference of the two is shown in the bottom frame.

$$A_y \approx \frac{1}{P_t} \frac{\sigma_\uparrow - \sigma_\downarrow}{\sigma_\uparrow + \sigma_\downarrow} \quad (4)$$

therefore the asymmetry in the elastic peak is definitely large and the background is either unpolarized or has an analyzing power of approximately zero.

The data were obtained in 3–4 h sets with polarization measurements immediately prior to and after each set. The polarization value used for a particular data set was the average of these two values and only data sets with an average polarization of 0.4 or larger were analyzed. Also, the data sets during which a large (> 10%) decrease in the polarization was observed (see Fig. 3) were not used, since the polarization loss may have occurred suddenly at any point during the run or it may have been constant throughout the run. The additional uncertainty in these cases would be one-half of the difference in the polarization values. The polarization was reversed every 12 h. Therefore several data sets were obtained for each angle and polarization state. This results in an overdetermined set of equations from which the asymmetry and cross section were extracted by a least squares minimization of the function

$$\chi^2 = \sum_i \frac{[\sigma_i - \sigma_o(1 + A_y P_{t_i})]^2}{(\Delta\sigma_i)^2} \quad (5)$$

Here,  $\sigma$  and  $\sigma_o$  are the measured polarized and unpolarized cross sections, respectively,  $P_t$  is the target polarization,  $A_y$  is the analyzing power, and the sum is over individual data sets  $i$ . The results are presented in Ta-

bles I and II with the first error arising from counting statistics and the second from systematic uncertainties.

#### IV. DISCUSSION

Measured angular distributions of  $d\sigma/d\Omega$  and  $A_y$  for  $\pi^+$ - $^3\text{He}$  elastic scattering at 100 MeV are presented in Table I and are shown in Fig. 9 along with accurate cross section data of Källne *et al.* [14]. The error bars shown represent the statistical uncertainties only. The data points at  $60^\circ$  and  $100^\circ$  are from Ref. [18]. The  $80^\circ$  point is the average of the values obtained from phase one [18] and phase two. In Fig. 9 the data are compared to the full DWIA calculation of Ref. [9] (solid curve), the DWIA calculation with only the  $S$ -state component of the  $^3\text{He}$  wave function included (dashed line), and the same calculation with the full  $^3\text{He}$  wave function and a  $\rho^2$  term in the optical potential (dotted line). The  $\rho^2$  term is included to account for true pion absorption and second-order effects. The similarity between the solid and dashed curves of Fig. 9 (top frame) indicates that the asymmetry is insensitive to  $^3\text{He}$  nuclear structure details. This feature is not unexpected since the  $^3\text{He}$  form factor cancels out of the asymmetry in the simple PWIA model [19] which is described below for the case of  $\pi^-$ - $^3\text{He}$  elastic scattering. The attempt to include absorption also yields little change from the first-order DWIA pre-

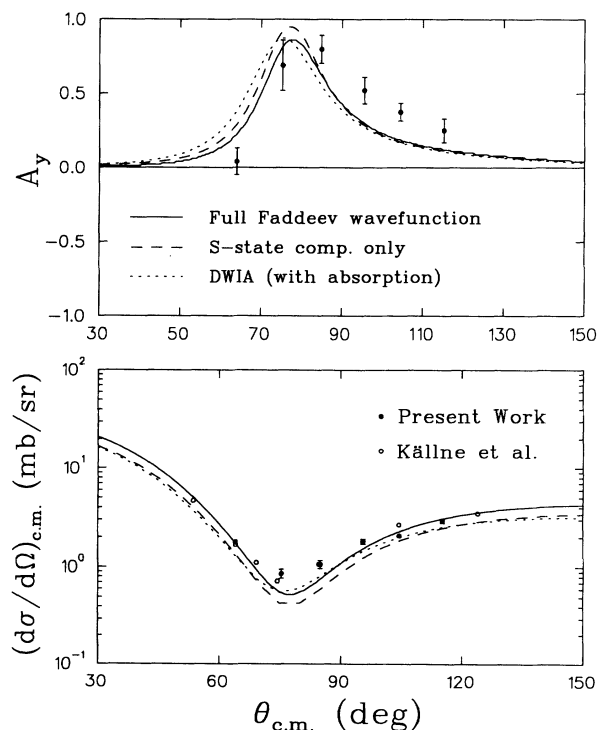


FIG. 9.  $A_y$  (top) and cross section (bottom) angular distributions for the  $\pi^+$ - $^3\text{He}$  elastic scattering at 100 MeV. The data are compared to three full nonlocal DWIA calculations using Faddeev wave functions for  $^3\text{He}$ .

diction and, in fact, results in worse agreement with the data. This is an indication that the current method of incorporating second-order effects via the  $\rho^2$  term, which was developed for heavy nuclei, is perhaps not appropriate for  ${}^3\text{He}$ . From comparisons of the data set of phase one to the full DWIA calculation and the simple PWIA calculation [18,19] it was determined that multiple scattering effects were important in  $\pi^+{}^{-3}\text{He}$  scattering at 100 MeV. The DWIA calculation yielded significantly better agreement with that data, especially at the largest angle. With the new data points, it is clear that the DWIA calculation still underestimates the asymmetry at large angles.

The boost needed to bring the theoretical asymmetry up to the level of the data at large angles is similar in magnitude to the level of improvement obtained with the DWIA model including the full Faddeev wave function relative to the PWIA model. The difference between the two calculations occurs mainly in the imaginary part of the spin-flip amplitude [19]. In fact, the full DWIA calculation gives an enhancement of a factor of 2–3 in the spin-flip amplitude relative to the PWIA model. This enhancement also has a large effect on the cross section in the region of the cross section minimum (where the spin-flip amplitude is large) providing a factor of  $\sim 1.7$  increase in  $\sigma$ . This enhancement is still not sufficient to bring the theory up to the level of the data however.

In Fig. 10 we compare our measured angular distributions of  $d\sigma/d\Omega$  and  $A_y$  for  $\pi^-{}^{-3}\text{He}$  elastic scattering at 100 MeV with the DWIA calculation mentioned above (solid line), and two simple PWIA calculations which are outlined below. In the PWIA model of Ref. [19], the non-spin-flip ( $\tilde{F}$ ) and spin-flip ( $\tilde{G}$ ) amplitudes for  $\pi^-{}^{-3}\text{He}$  scattering are given by

$$\tilde{F}_- = (2f_{\pi^-p} + f_{\pi^-n})F_{J=0}(Q^2), \quad (6)$$

$$\tilde{G}_- = g_{\pi^-n}F_{J=1}(Q^2), \quad (7)$$

where  $f_{\pi^-p,n}$  are the elementary  $\pi^-N$  amplitudes [21] and it is assumed that  $F_{J=0}(Q^2) = F_{J=1}(Q^2) = \exp(-r_0^2 Q^2/6)$ . The value assumed for  $r_0$  was 1.65 fm. This model is represented by the dashed line of Fig. 10. Since the cross section for  $\pi^-n$  scattering is about six times larger than that for  $\pi^-p$  scattering (at  $80^\circ$  c.m.) it may also be a reasonable approximation to assume that the asymmetry is due only to scattering from the neutron, i.e.,

$$\tilde{F}_-^n = f_{\pi^-n}F_{J=0}(Q^2), \quad (8)$$

$$\tilde{G}_-^n = g_{\pi^-n}F_{J=1}(Q^2). \quad (9)$$

This calculation [22] is plotted as the dotted line in Fig. 10.

In general the asymmetries here are almost a factor of 2 smaller than for  $\pi^+$  scattering and greatly resemble the asymmetries for  $\pi^-n$  scattering near the cross section minimum where the spin-flip amplitude is dominant. Recalling the expression  $A_y \equiv 2|\tilde{F}||\tilde{G}|\sin(\Delta\theta)/\sigma_o$  where  $\sigma_o \equiv |\tilde{F}|^2 + |\tilde{G}|^2$  it is evident that the spin-flip and non-

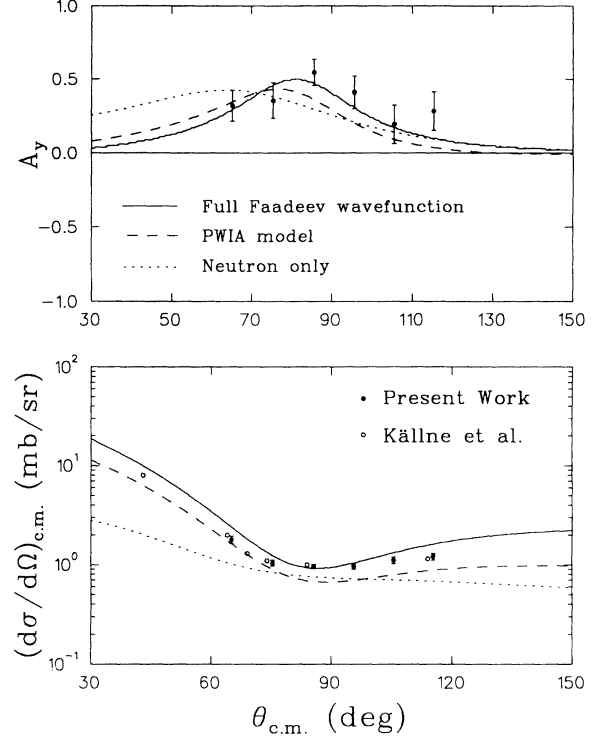


FIG. 10.  $A_y$  (top) and cross section (bottom) angular distributions for  $\pi^-{}^{-3}\text{He}$  elastic scattering at 100 MeV. The data are compared to a full DWIA calculation (solid curve) and the two PWIA models (dashed and dotted curves) outlined in the main text.

spin-flip amplitudes must be of roughly equal magnitude and must interfere constructively in order for the resulting asymmetry to approach unity. This was clearly the case for  $\pi^+{}^{-3}\text{He}$  scattering near  $\theta_{c.m.} = 80^\circ$ . In the case of  $\pi^-{}^{-3}\text{He}$  scattering however, the elementary  $\pi^-n$  spin-flip amplitude is much larger in the region of the cross section minimum ( $g_{\pi^-n} \approx 3g_{\pi^+n}$ ), therefore the equality criterion is not as well satisfied and the asymmetry is reduced.

In general, agreement between theory and data is better for  $\pi^-$  scattering than for  $\pi^+$  scattering for both  $\sigma$  and  $A_y$ . There is still an indication that the DWIA calculation underpredicts the asymmetry at large angles although the theory is just within one standard deviation of the data. Cross sections are well predicted by theory in this case even in the region of the cross section minimum. This is likely due to the fact that a single elementary amplitude ( $g_{\pi^-n}$ ) is dominant here. Also, since there is only one neutron, the importance of multiple scattering effects should be reduced in this region relative to  $\pi^+{}^{-3}\text{He}$  scattering.

## V. CONCLUSION

In summary, we have presented measurements of  $\sigma$  and  $A_y$  in elastic scattering of both  $\pi^+$  and  $\pi^-$  from polarized  ${}^3\text{He}$ . The measured asymmetries are large near the

cross section minima ( $\sim 70^\circ$ – $80^\circ$ ) and the angular distributions are in qualitative agreement with the theory. The asymmetry measured in  $\pi^-$  scattering is about half as large as in the  $\pi^+$  case and is also in fair agreement with theoretical calculations.

In elastic  $\pi^\pm$ - $^3\text{He}$  scattering at 100 MeV the asymmetries show a distinct lack of sensitivity to nuclear structure details. Sensitivity to the reaction mechanism is indicated in the improved agreement between theory and data obtained when multiple scattering is included in the reaction model. However, the full DWIA calculation still underpredicts the asymmetry at backward angles, most noticeably for  $\pi^+$ - $^3\text{He}$  scattering. The discrepancies between the DWIA predictions and the data, both in the asymmetry at backward angles and in the cross section near the minimum, are indications that the spin-flip amplitude is not being calculated well enough. The current method of modeling true pion absorption and second-order effects in the DWIA calculation results in a larger discrepancy between the theoretical calculation and the data although the effect is very small at backward angles.

In the case of  $\pi^-$  scattering, both the cross section and the asymmetry are insensitive to the reaction model in the region of the cross section minimum where the spin-flip amplitude for scattering from the lone neutron

is dominant. The asymmetry does provide some sensitivity at large angles where the full nonlocal DWIA calculation seems generally lower than the data as was the case for  $\pi^+$ - $^3\text{He}$  scattering but with a reduced level of significance. Together, the cross section and asymmetry measurements provide complementary information on the spin-flip amplitude and yield sensitivity to the reaction model over a wide range of scattering angles.

At energies above the  $\Delta$  resonance the model dependence of the asymmetry is greatly enhanced. The full calculation of Ref. [9] predicts a dramatic sign reversal for the analyzing power in this energy region whereas the simple model described in Sec. IV predicts that the asymmetry remains large and positive. The exact energy at which the asymmetry changes sign is also very sensitive to the inclusion of a true pion absorption term [19]. Measurements of the analyzing power at higher energies will therefore provide extremely sensitive tests of the  $\pi$ - $^3\text{He}$  reaction mechanism. An experiment which will measure the analyzing power in pion elastic scattering from polarized  $^3\text{He}$  at energies above 100 MeV has recently been completed at LAMPF [23].

This work was supported by grants from the Natural Sciences and Engineering Research Council of Canada.

- 
- [1] R.H. Landau, S.C. Pathak, and F. Tabakin, *Ann. Phys. (N.Y.)* **78**, 299 (1973).
  - [2] R.H. Landau and A.W. Thomas, *Nucl. Phys.* **A302**, 461 (1978).
  - [3] R. Mach, *Nucl. Phys.* **A258**, 513 (1976).
  - [4] R.H. Landau, *Phys. Rev. C* **15**, 2127 (1977).
  - [5] M. Wakamatsu, *Nucl. Phys.* **A340**, 289 (1980).
  - [6] D.J. Ernst, in *Proceedings of the LAMPF Workshop on Physics with Polarized Targets*, Los Alamos, New Mexico, 1986 (LANL Report No. LA-10772-C, 1986), p. 129.
  - [7] F.M.M. Van Geffen, B.L.G. Bakker, H.J. Boersma, and R. Van Wageningen, *Nucl. Phys.* **A468**, 683 (1987).
  - [8] R. Mach and S.S. Kamalov, *Nucl. Phys.* **A511**, 601 (1990).
  - [9] S.S. Kamalov, L. Tiator, and C. Bennhold, *Few Body Systems* **10**, 143 (1991); *Phys. Rev. C* **47**, 941 (1993).
  - [10] R. Tacik *et al.*, *Phys. Rev. Lett.* **63**, 1784 (1989).
  - [11] Yi-Fen Yen *et al.*, *Phys. Rev. Lett.* **66**, 1959 (1991).
  - [12] B. Larson, O. Häusser, P.P.J. Delheij, D.M. Whittal, and D. Thiessen, *Phys. Rev. A* **44**, 3108 (1991).
  - [13] J. Källne *et al.*, *Phys. Rev. Lett.* **45**, 517 (1980).
  - [14] J. Källne, J.F. Davis, J.S. McCarthy, R.C. Minehart, R.R. Whitney, R.L. Boudrie, J.B. McClelland, and A. Stetz, *Phys. Lett.* **103B**, 13 (1981).
  - [15] G. Fournier, A. Gérard, J. Miller, J. Picard, B. Saghai, P. Vernin, P.Y. Bertin, B. Coupât, E.W.A. Lingeman, and Kamal K. Seth, *Nucl. Phys.* **A426**, 542 (1984).
  - [16] R.S. Hicks, J. Dubach, R.A. Lindgren, B. Parker, and G.A. Peterson, *Phys. Rev. C* **26**, 339 (1982).
  - [17] R.A. Brandenburg, Y.E. Kim, and A. Tabis, *Phys. Rev. C* **12**, 1368 (1975).
  - [18] B. Larson *et al.*, *Phys. Rev. Lett.* **67**, 3356 (1991).
  - [19] C. Bennhold, B.K. Jennings, L. Tiator, and S.S. Kamalov, *Nucl. Phys.* **A540**, 621 (1992).
  - [20] R.J. Sobie *et al.*, *Nucl. Instrum. Methods* **219**, 501 (1984).
  - [21] R.A. Arndt and L.D. Soper, SAID program,  $\pi N$  scattering solutions (unpublished).
  - [22] B.K. Jennings, private communication.
  - [23] LAMPF Experiment 1267, D. Dehnhard, G. Burlison, and O. Häusser spokesmen.